J. Fluid Mech. (2025), *vol.* 1018, A44, doi:10.1017/jfm.2025.10561

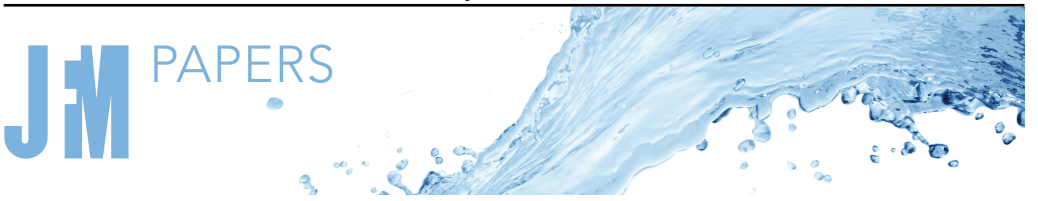

A fully nonlinear solution of the flow around a spinning spheroid in a rotating stratified fluid

Antoine Chauchat[1], **Michael Le Bars**[1] **and Patrice Meunier**[1]

[1]CNRS, Aix Marseille Univ, Centrale Marseille, IRPHE, Marseille 13013, France

Corresponding authors: Antoine Chauchat, antoinechauchat@gmail.com;
Michael Le Bars, michael.le-bars@univ-amu.fr; Patrice Meunier, meunier@irphe.univ-mrs.fr

(Received 14 March 2025; revised 2 July 2025; accepted 5 August 2025)

This paper investigates the flow and density field around a spinning solid spheroid with a given aspect ratio, immersed in a rotating stratified fluid. First, we derive the general system of equations governing such flows around any solid of revolution in the limit of infinite Schmidt number. We then present an exact analytical solution for a spinning spheroid of arbitrary aspect ratio. For the specific case of a sphere, we provide the diffusive spin-up solution obtained via an inverse Laplace integral. To validate the theoretical results, we experimentally reproduce these flows by spinning spheroids in a rotating tank filled with stratified salt water. By varying the stratification intensity, the angular velocities of the spheroid and the rotating table, and the spheroid's shape, we explore a broad parameter space defined by Froude, Reynolds and Rossby numbers and aspect ratio. Using particle image velocimetry to measure the velocity field, we demonstrate excellent agreement between theory and experiments across all tested regimes.

Key words: rotating flows, stratified flows, vortex flows

1. Introduction

Rotating stratified flows are a key element in geophysical fluid dynamics. For example, the warm and salty Mediterranean water can flow into the Atlantic Ocean and form vortices called meddies, short for Mediterranean eddies. Meddies can live up to four years (Armi *et al.* 1989; Bashmachnikov *et al.* 2015). They are typically 1 km high and 100 km long (Richardson, Bower & Zenk 2000). Similar mesoscale eddies are observed in different locations (Meschanov & Shapiro 1998; Chang *et al.* 2004; Carton *et al.* 2013). Meddies adopt a spheroidal shape whose aspect ratio depends on the competition between rotation and the difference between the core and the ambient stratification (Aubert *et al.* 2012).

The flow around deep ocean vortices like meddies destabilises into layers (Hua *et al.* 2013). These homogeneous layers break locally the density gradient and may contribute to mixing in the oceans (Ruddick & Hebert 1988; Molemaker, Mcwilliams & Capet 2010). The role of these instabilities is thus of primary importance for the global fluxes of temperature and carbon dioxide. To describe the instabilities around meddies, numerical (Yim, Billant & Ménesguen 2016; Sutyrin & Radko 2017; Le Bars 2021) and experimental (Saunders 1973; Griffiths & Linden 1981; Burin, Sommeria & Viboud 2020) studies have been conducted. However, at scales accessible in the laboratory, spheroidal fluid vortices tend to be rapidly damped by viscosity and the growth rate of the instabilities can be similar to the lifetime of the vortex. It is thus difficult to get reliable results on the mechanisms at play.

To study the instabilities around columnar vortices, numerous studies have replaced the fluid vortex by a solid cylinder spinning in a stratified fluid. Numerical studies (Smyth & McWilliams 1998; Kloosterziel, Carnevale & Orlandi 2007; Yim & Billant 2015) are complemented by experimental (Le Bars & Le Gal 2007; Riedinger, Le Dizès & Meunier 2011; Flór *et al.* 2018) studies in cylindrical Taylor–Couette geometries. Likewise, the flow in a meddy core can be approximated by a solid-body rotation (Paillet *et al.* 2002; Tokos & Rossby 1991). A spinning spheroid in a rotating stratified fluid is thus a good candidate for experimental studies of the instabilities around meddies.

It is first necessary to know the base flow which is the subject of the present paper. The Stokes velocity profile induced by a spinning spheroid in a uniform non-rotating fluid has been computed by Jeffery (1915) using spheroidal coordinates. In the absence of background stratification this Stokes flow creates vertical velocities by Ekman pumping at finite Reynolds number (Marcus & Tuckerman 1987), leading to a meridional recirculation. The full nonlinear Navier–Stokes solution around a spinning spheroid is thus unknown in a homogeneous fluid. In this paper, we generalise the Stokes flow solution to any Reynolds number and any Rossby number by allowing the fluid to be stratified and compute the density anomaly induced by the flow.

In § 2 we present the experimental set-up and the measurement techniques. In § 3 we propose a simplified set of equations describing the flow around a spinning solid of any arbitrary shape in a rotating stratified fluid. In § 4, those equations are solved in the case of a sphere and compared with experimental results. The spin-up of the flow around a sphere is also analytically described. In § 5, the equations are solved around prolate and oblate spheroids by use of spheroidal coordinates and compared with experiments. We then conclude in § 6 with the prospects brought by this study.

2. Materials and methods

2.1. *Experimental set-up*

The experiments are performed in a cylindrical tank of 1 m in diameter and 1.6 m in height. Figure 1(*a*) shows a photograph of the experimental set-up. Figure 1(*b*) shows a schematic. The laser can be translated vertically to scan different heights of the flow. The tank is mounted on a table rotating at angular speed Ω ranging from 0 to 4.7 rad s^{-1}. Different spheroids of $R = 4$ cm in radius and respective heights $2H$ of 16, 8, 4 and 1 cm can be mounted on a spinning axis placed in the centre of the tank. The tank is filled with a top layer of clear water. Then an intermediate linearly stratified layer is introduced below the clear water via the double-bucket technique. Finally a bottom layer of nearly saturated salt water is introduced below the stratified layer. Following Nayar *et al.* (2016), viscosity is taken equal to 1.2×10^{-6} m^2 s^{-1} at the centre of the stratified layer. The spheroid is placed in the middle of the stratified region as shown in figure 1(*b*). A stepper motor spins

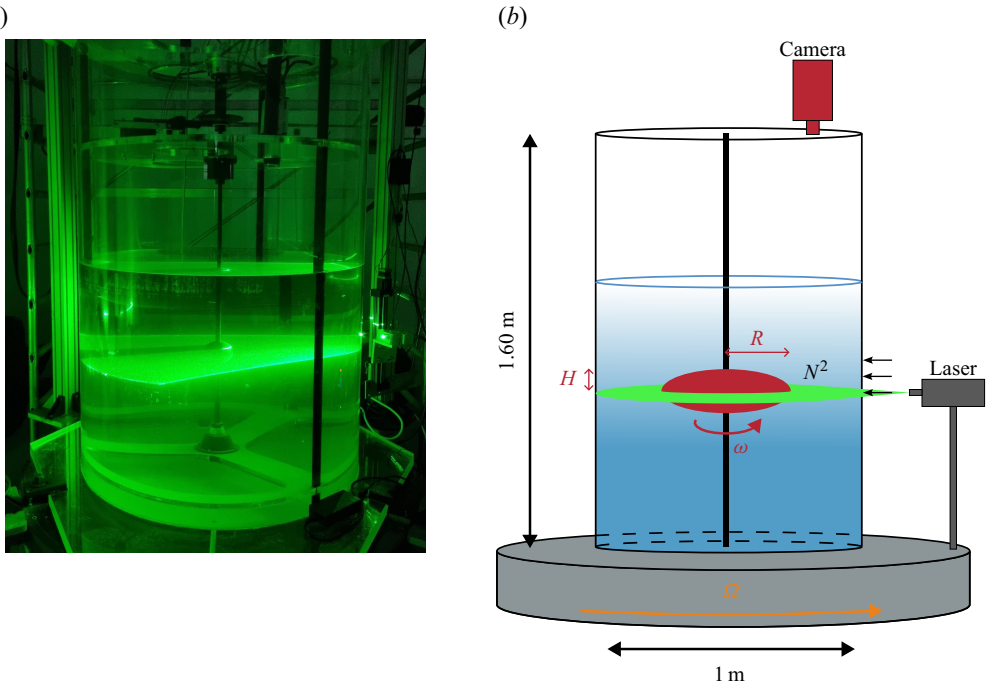

Figure 1. Photograph (*a*) and schematic (*b*) of the experimental set-up. As suggested by the arrows, the laser can be vertically translated to scan different heights of the flow.

the spheroid at angular speed ω ranging from 0 to 4.7 rad s^{-1} in the rotating frame of the table in either co-rotation or contra-rotation. The spinning spheroid sets the fluid into an azimuthal motion that remains axisymmetric for small enough rotation rates.

2.2. *Density measurements*

The density has been measured to check that the stratification profile is linear in height around the spheroid and to compute the Brunt–Väisälä angular frequency. Samples of the fluid are taken at different heights and their densities are measured with an oscillating U-tube densimeter. A typical stratification profile is given in figure 2. This profile shows that the fluid is separated in three regions. The upper one is filled with clear water. The middle one is linearly stably stratified. The bottom one is filled with salted water. Between those main regions there are smaller transition regions due to mixing during the filling of the tank and to salt diffusion afterwards. The linear regression in the stratified domain yields the vertical density gradient and then the Brunt–Väisälä angular frequency with the usual definition: $N^2 = -(g/\rho_0)(\mathrm{d}\bar{\rho}^*/\mathrm{d}z^*)$, for this particular profile, $N = 2.04$ rad s^{-1}. The ratio between the size of the stratified region and the full height of the spheroid varies from 1.25 for the longest spheroid to 20 for the flattest.

2.3. *Particle image velocimetry measurements*

Particle image velocimetry (PIV) is used to measure azimuthal velocities in the fluid. The two buckets used to fill the stratified region are seeded with hollow glass particles of 10 μm in diameter and density close to 1 g cm^{-3}. A nearly horizontal green laser sheet illuminates the tank. To scan different heights the laser is mounted on a vertical translation platform. A high-resolution camera is focused on the laser plane with a field of view of about

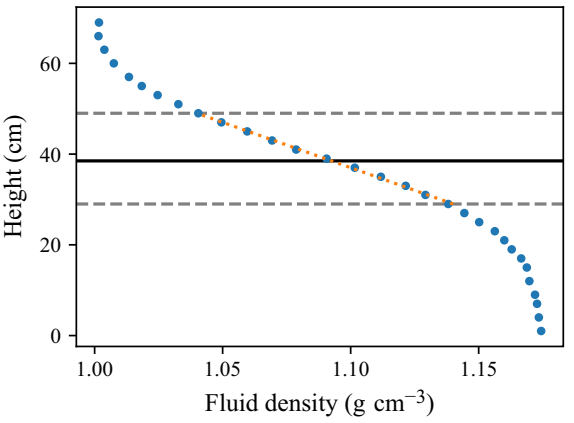

Figure 2. Typical stratification profile. The top region is full of fresh water. The middle region is stably stratified in salt concentration. The bottom region is full of salt water. The dark line indicates the height of the equator of the spheroid. Between the two dashed lines the profile is linear. The orange dotted line is a linear regression through which we compute the density gradient and deduce the Brunt–Väisälä angular frequency $N = 2.04\,\mathrm{rad\,s^{-1}}$.

8 spheroid radii along one axis and 6 along the other. We thus have access to the full three-dimensional dependence of the stationary azimuthal flow around the spheroids. Because of the salt concentration stratification, the middle layer is also stratified in optical index. The laser sheet is thus slightly bent downwards in a parabolic shape. This is compensated by inclining the laser with a small upward angle so that the maximum of the parabola is in the middle of the field of view of the camera. The maximum of vertical deviation between the centre of the plane and the edge is only a couple of millimetres. The sheet is thus considered flat in the field of view of the camera. Velocity profiles are computed by projecting the flow in the azimuthal direction and averaging over every visible angle for each radial distance. All velocity measurements of the steady flow are taken after the transient for a time greater than 60 diffusive times.

3. A simple azimuthal flow solution

3.1. *Governing equations*

The flow in the rotating frame of the table around the spheroid in the stratified region is taken to be incompressible. The Navier–Stokes equations in the Boussinesq approximation and the conservation of salt in dimensional variables are

$$\frac{\partial \boldsymbol{v}^*}{\partial t^*} + (\boldsymbol{v}^* \cdot \nabla^*)\boldsymbol{v}^* + \Omega^2 \boldsymbol{r}^* + 2\boldsymbol{\Omega} \times \boldsymbol{v}^* = -\frac{1}{\rho_0}\nabla^* p_t^* - \frac{\rho_t^*}{\rho_0} g\hat{z} + \nu \nabla^{*2} \boldsymbol{v}^*, \tag{3.1}$$

$$\nabla^* \cdot \boldsymbol{v}^* = 0, \tag{3.2}$$

$$\frac{\partial \rho_t^*}{\partial t^*} + \boldsymbol{v}^* \cdot \nabla^* \rho_t^* = D \nabla^{*2} \rho_t^*. \tag{3.3}$$

Here, $\boldsymbol{r}^*$ corresponds to the horizontal position vector.

The density is decomposed into the reference density, the density due to the stratification and the dynamical density due to the flow, $\rho_t^* = \rho_0 + \bar{\rho}^* + \rho^*$ with $\bar{\rho}^* = -\rho_0 N^2 z^*/g$. The pressure is decomposed accordingly into the atmospheric pressure, the hydrostatic pressure that equilibrates the reference density and the stratification density, the pressure due to the centrifugal force $\rho_0 \Omega^2 r^{*2}/2$ and the dynamical pressure due to the flow, $p_t^* = P_0 + p_0 + \bar{p}^* + p_c^* + p^*$.

The time scale is taken as the diffusive time R^2/ν, the length scale as R and the velocity scale as ωR. The pressure scale is $\rho_0(\omega R)^2$ and the density scale is the variation in density $\rho_0(RN^2/g)$ over a distance R. Equations (3.1)–(3.3) read in dimensionless form:

$$\frac{1}{Re}\frac{\partial \boldsymbol{v}}{\partial t} + (\boldsymbol{v}\cdot\boldsymbol{\nabla})\boldsymbol{v} + \frac{2}{Ro}\hat{z}\times\boldsymbol{v} = -\boldsymbol{\nabla}p - \frac{1}{Fr^2}\rho\hat{z} + \frac{1}{Re}\nabla^2\boldsymbol{v}, \tag{3.4}$$

$$\boldsymbol{\nabla}\cdot\boldsymbol{v} = 0, \tag{3.5}$$

$$\frac{1}{Re}\frac{\partial \rho}{\partial t} + \boldsymbol{v}\cdot\boldsymbol{\nabla}\rho = \frac{1}{Sc}\nabla^2\rho. \tag{3.6}$$

In the experiments, the Reynolds number $Re = \omega R^2/\nu$ ranges from 500 to 1000, the Froude number $Fr = \omega/N$ ranges from 0.16 to 0.32 and the Rossby number $Ro = \omega/\Omega$ is equal to -1, 6 and infinity. The Schmidt number $Sc = \nu/D$ is equal to 700. The aspect ratio $\Lambda = H/R$, where H is the half-height of the spheroid, appears in the boundary conditions and ranges in the experiments from 0.5 to 2.

3.2. *Generic set of equations valid around any rotating solid of revolution*

For a homogeneous fluid ($\rho = 0$), the solution to the Navier–Stokes equations (3.4) is difficult to find since the vertical and radial velocities are generated by Ekman pumping. However, for a stratified fluid it is possible to get a time-independent axisymmetric flow with a purely azimuthal velocity. Let us look in cylindrical coordinates (r, z, ϕ) for a solution $\boldsymbol{v} = v(r,z)\hat{\boldsymbol{\phi}}$, $p = p(r,z)$, $\rho = \rho(r,z)$. The boundary conditions read $v(\text{on the solid}) = r$, $v(\infty) = 0$ and $p(\infty) = 0$. They imply $\rho(\infty) = 0$. The continuity equation (3.5) is satisfied and the conservation of salt (3.6) is satisfied in the large-Sc limit. We take this limit given that $Sc = 700$ for salt water. Equation (3.4) gives the three momentum equations that are left for our three scalar variables:

$$\nabla^2 v - \frac{v}{r^2} = 0, \tag{3.7}$$

$$\frac{\partial p}{\partial r} = \frac{v^2}{r} + \frac{2}{Ro}v, \tag{3.8}$$

$$\rho = -Fr^2\frac{\partial p}{\partial z}. \tag{3.9}$$

Equation (3.7) indicates that the Stokes flow, obtained at vanishing Reynolds number as a solution of the vector Laplacian equal to 0, is still a valid base flow for any Reynolds number.

Surprisingly, the velocity field does not depend on Fr, Ro and Re and depends only on the shape of the solid.

In the presence of stratification, this flow is an exact steady solution of the nonlinear equations. Indeed, in (3.8), the azimuthal centrifugal and Coriolis terms are balanced by a radial pressure gradient that imposes the solution to the full pressure field. It induces a vertical pressure gradient, which is balanced in (3.9) by the variable density. This density field, that prevents the addition of a vertical velocity, comes from the deflection of the isopycnals and is only present in the case of a stratified fluid. While the velocity field depend only on the shape of the solid, because of the Coriolis term the density profile depends on the shape of the spheroid, the Froude number and the Rossby number. In other words, in the absence of stratification, the azimuthal velocity would induce recirculation by Ekman pumping on the boundary of the solid. Here, the density perturbation ρ is proportional to Fr^2. When the Froude number increases, the density gradient $\partial\rho/\partial z$ increases and may become larger than the mean density gradient $\mathrm{d}\bar{\rho}/\mathrm{d}z = -1$, leading

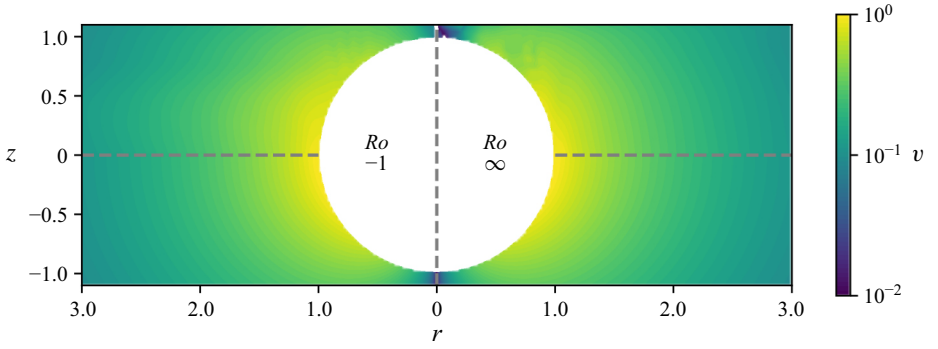

Figure 3. Velocity colourmap around a spinning sphere. The bottom region is the theoretical base flow computed from (4.1). The top region is an interpolation of experimental velocity profiles at different heights. On the left, $Re = 804$, $Fr = 0.296$, $Ro = -1$. On the right, $Re = 1005$, $Fr = 0.306$, $Ro = \infty$.

to convectively unstable regions. Therefore, this solution, although valid for any Froude number, becomes irrelevant for large Froude numbers, i.e. weak stratifications. Let us note that this flow is not restricted to linear stratification profiles but valid for any background stratification profile. Note that we do not pretend that this solution remains stable for any Reynolds, Rossby or Froude number. For high Reynolds number the flow may be considered as a destabilisation of this base flow.

4. Flow around a sphere

4.1. *Stationary flow*

Around a sphere in an infinite medium, the Stokes flow solution of (3.7) is given by Jeffery (1915) in spherical coordinates (μ, θ, ϕ):

$$v = \frac{\sin\theta}{\mu^2}. \tag{4.1}$$

Figure 3 shows a colourmap of the velocity field around a spinning sphere. The top region is an experimental interpolation from profiles at different heights. The bottom region is the theoretical velocity computed from (4.1). There is no global background rotation on the right and a strong contra-rotation on the left which does not modify the azimuthal velocity. There is a very good agreement between the experiments and the theory in both cases. The discrepancies between the two plots come from the logarithmic scale enhancing any PIV error and the difference of vertical sampling leading to a different interpolation and spurious isovelocity contours. Let us highlight that this is not a low-Re flow, $Re \simeq 1000$, as the advective terms do not need to be neglected because of their geometric cancellation.

More quantitatively, an experimental validation of the flow up to 8 radii is shown in figure 4. At each height the velocity is plotted and compared with the theoretical velocity. There is an excellent agreement between the experiments and the theory for both $Ro = \infty$ and $Ro = -1$. Given that the flow does not depend on the Rossby number and that it is gravitationally stable for low Froude numbers, this agreement is expected to hold in the geophysical regime where $|Ro| \ll 1$.

The pressure may be found by rewriting the velocity profile given by (4.1) in cylindrical coordinates, introducing it in (3.8) and integrating with respect to r. However, it is easier to rewrite the term $(\partial p/\partial r)_z$ on the left-hand side of (3.8) using spherical coordinates, as given in Appendix A by (A2). Formally we locate a point in space using their spherical

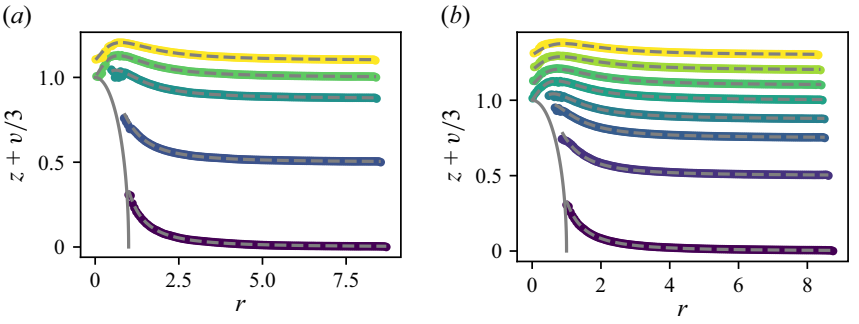

Figure 4. Theoretical and experimental azimuthal velocity radial profiles around a spinning sphere. Circles are PIV measurements. Dashed lines are the analytical base flow (4.1) at each height, which has no fitting parameter and does not depend on any dimensionless number. The profiles are shifted by their height and scaled by a factor of 1/3 to distinguish them. (*a*) From dark to light, the heights are $z = 0,\ 0.5,\ 0.875,\ 1$ and 1.1 with $Ro = \infty,\ Re = 1005,\ Fr = 0.306$. (*b*) From dark to light, the heights are $z = 0,\ 0.5,\ 0.75,\ 0.875,\ 1,\ 1.1,\ 1.2$ and 1.3 with $Ro = -1,\ Re = 804,\ Fr = 0.296$.

distance to the origin μ, their height z and their azimuthal angle ϕ. We thus use the mixed coordinates (μ, z, ϕ). Equation (3.8) is simply written

$$\sin\theta \left(\frac{\partial p}{\partial \mu}\right)_z = \frac{v^2}{\mu \sin\theta} + \frac{2}{Ro} v. \tag{4.2}$$

Since v is proportional to $\sin\theta$, the θ dependence disappears from this equation and it can be easily integrated in μ to give

$$p = \frac{-1}{4\mu^4} - \frac{2}{Ro\mu}. \tag{4.3}$$

The density can be found by noting that the pressure gradient $(\partial p/\partial z)_r$ on the right-hand side of (3.9) is equal to $\cos\theta(\partial p/\partial \mu)_r$ (see Appendix A). Equation (3.9) thus gives

$$\rho = -Fr^2 \cos\theta \left(\frac{1}{\mu^5} + \frac{2}{Ro\mu^2}\right). \tag{4.4}$$

Contrary to the velocity, the density field depends on both the Froude and the Rossby numbers, as shown in figure 5. We here plot the full variable density profile $\bar{\rho} + \rho$. The isopycnals in the full space can be obtained by symmetrising any quadrant with respect to the vertical and horizontal axes. In the upper right quadrant we see that without background rotation the flow tends to bend isopycnals towards the equator with an increased effect near the poles. This can be understood because if there was no deflection, the pressure would induce Ekman pumping that would advect the isopycnals from the poles to the equator and create a deflection. The equilibrium is reached when the buoyancy force counterbalances the pressure gradient. When decreasing the stratification strength, i.e. increasing Fr, the isopycnals bend more, as shown in the upper left corner. This can create regions near the poles with overturning. The lower left corner shows that co-rotation exacerbates the bending far from the sphere. On the other hand, the lower right corner shows that contra-rotation ($Ro < 0$) tends to bend the isopycnals the other way around and suppress the overturn. Let us note that the isopycnals are not necessarily orthogonal to the solid surface because we have taken the large-Sc limit. A molecular diffusive boundary layer is probably present in the experiment.

Let us remark that by neglecting diffusion of density, the density can only be advected during the spin-up to produce the equilibrium profile. On the axis of rotation only a vertical velocity may advect this density meaning that the transient cannot lead to a profile where

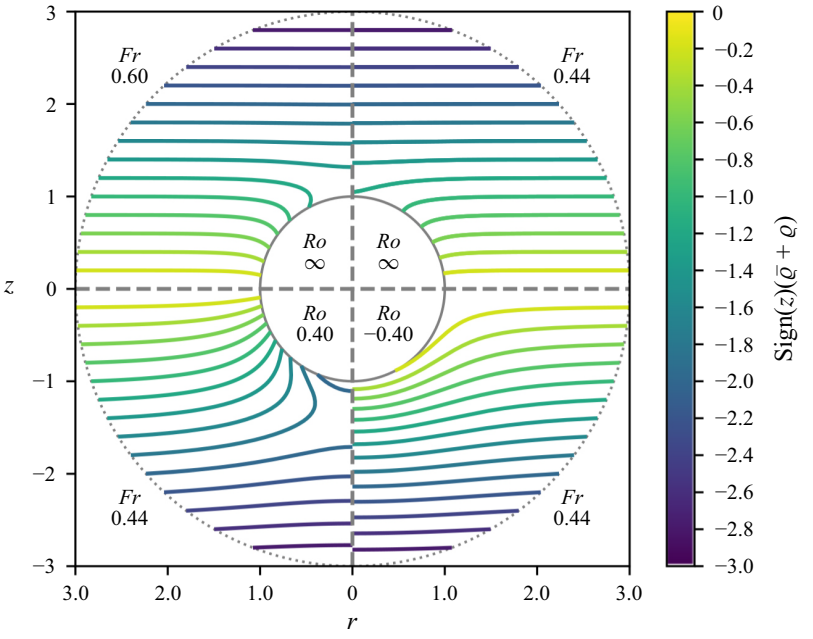

Figure 5. Theoretical isopycnals from (4.4) around a spinning sphere for four sets of *Ro* and *Fr* values. Each quadrant corresponds to a pair of *Ro* and *Fr*. In the upper (lower) region the density is increasing (decreasing) from dark to light. The dotted outer sphere is not a boundary but only the end of the plotting region.

the total vertical density gradient is positive. Setting $\partial\rho/\partial z = 1$ and $z = 1$ yields the critical Froude number where that overturning occurs. Overturning occurs when $Ro < -4/5$ or $Ro > 0$ and $Fr^2 > 1/(5 + 4/Ro)$. For a high enough Froude number this base flow cannot establish and vertical and radial velocities will be present. The same reasoning applies on the equator and it follows that overturning occurs at the equator for $0 > Ro > -2$ and $Fr^2 > 1/(1 + 2/Ro)$.

4.2. *Spin-up of the flow*

Initially, the solid and fluid are at rest in the rotating frame and the solid is instantaneously set spinning at angular frequency ω. The stratification inhibits vertical motions. We thus suppose that during the spin-up of the stationary flow, the velocity stays axisymmetric, azimuthal with the same co-latitude θ dependence $\boldsymbol{v} = (\sin\theta/\mu^2)\, f(t, \mu)$. We suppose that small- and fast-scale mechanisms that we do not need to describe ensure that the density profile is advected to balance this time-dependent flow. Then the azimuthal $\hat{\phi}$ component of the momentum equations reads

$$\frac{\partial f}{\partial t} = \frac{\partial^2 f}{\partial \mu^2} - \frac{2}{\mu}\frac{\partial f}{\partial \mu}. \tag{4.5}$$

The initial rest condition $f(t = 0^-, \mu) = 0$ and the boundary conditions $f(t, \mu = 1) = 1$ and $f(t, \mu \to \infty) = 0$ translate, respectively, in the Laplace domain to $\mathcal{L}(\partial_t f) = p\mathcal{L}(f)$, $\mathcal{L}(f)(p\mu = 1) = 1/p$ and $\mathcal{L}(f)(p, \mu \to \infty) = 0$. Equation (4.5) becomes $\mu^2 p\mathcal{L}(f) - \mu^2\partial_\mu^2\mathcal{L}(f) + 2\mu\partial_\mu f = 0$ which can be solved with the correct boundary conditions, leading to the analytical solution:

$$f(\mu, t) = \mathcal{L}^{-1}\left(\frac{\mathrm{e}^{-\sqrt{p}(\mu-1)}}{p}\,\frac{1 + \mu\sqrt{p}}{1 + \sqrt{p}}\right). \tag{4.6}$$

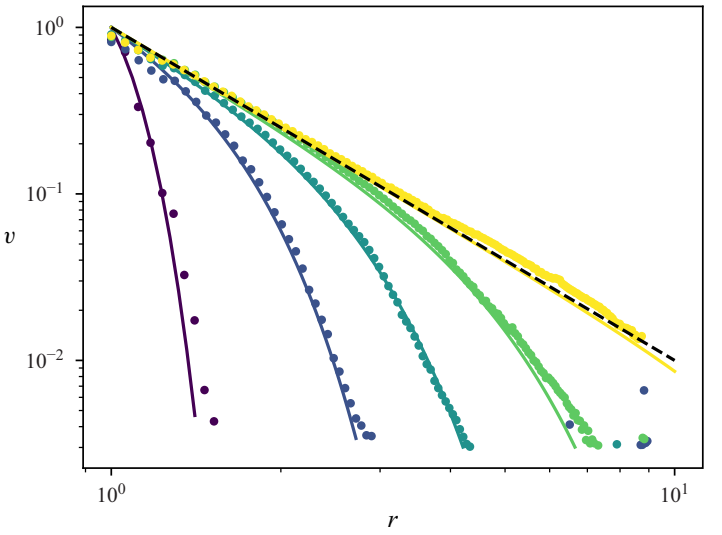

Figure 6. Theoretical and experimental azimuthal velocity radial profiles around a spinning sphere during spin-up. The velocities are measured and computed in the equatorial plane $z = 0$. The dashed line is the theoretical stationary profile. The plots from dark to light correspond to the diffusive times $t = 1.13 \times 10^{-2}$, 2.25×10^{-1}, 9×10^{-1}, 3.6 and 65.61. The circles are measurements from PIV. The lines are computed by the inverse Laplace transform. Here $Ro = \infty$, $Re = 503$, $Fr = 0.16$.

Numerically, the inverse Laplace transform is obtained using the instruction 'invertlaplace' in the Python library mpmath. It is plotted in figure 6 and compared with the experimental velocity during spin-up. The velocity is plotted in the equatorial plane where $\mu = r$. The PIV profiles are measured at different multiples of the diffusive time. At each time, (4.6) is computed to plot the theoretical flow. There is an excellent agreement between theory and experiments over two orders of magnitude of the velocity. The μ^{-2} dependence of the stationary flow is shown by the dashed black line of slope -2 in the log–log plot. This study of the transient flow shows that the flow stays axisymmetric and azimuthal in both transient and steady regimes. Let us note that Beckers *et al.* (2001) study in a similar fashion the decay of fluid pancake vortices. They model their vortices by Gaussian vortices and consider that no radial and vertical velocity is created during the decay. This leads to a pure diffusion of the azimuthal velocity over time. Similarly to our case, this simple model predicts well the temporal evolution of this flow.

5. Flow around a spheroid

5.1. *Prolate spheroid*

We can use the prolate spheroidal coordinates (μ, θ, ϕ) defined by $r = a \sinh\mu \sin\theta$ and $z = a \cosh\mu \cos\theta$, where $a = \sqrt{\Lambda^2 - 1}$ is the half-distance between the two foci of the spheroid. The flow around a prolate spheroid was given in Jeffery (1915) as

$$v = v_a \left[\coth\mu - \tanh^{-1}\left(\frac{1}{\cosh\mu}\right) \sinh\mu \right] \sin\theta \quad \text{with } v_a = \frac{1}{\Lambda - \tanh^{-1}(a/\Lambda)/a}. \tag{5.1}$$

Indeed, this solution satisfies (3.7) because the scalar Laplacian is equal to

$$\nabla^2 v = \frac{\partial_{\mu\mu} v + \partial_{\theta\theta} v + \coth\mu \partial_\mu v + \cot\theta \partial_\theta v}{a^2(\sinh^2\mu + \sin^2\theta)}. \tag{5.2}$$

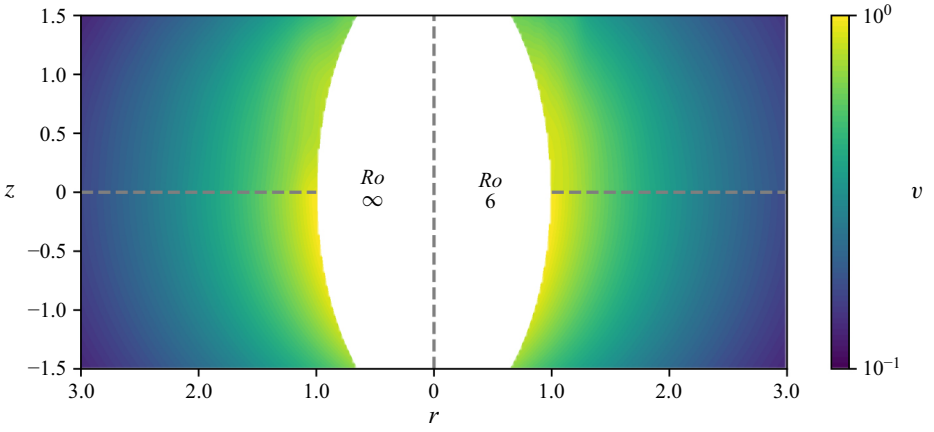

Figure 7. Velocity colourmap around a spinning spheroid of aspect ratio $\Lambda = 2$. The bottom region is the theoretical base flow computed from (5.1). The top region is an interpolation of experimental velocity profiles at different heights. On the left, $Re = 670$, $Fr = 0.320$, $Ro = \infty$. On the right, $Re = 838$, $Fr = 0.288$, $Ro = 6$.

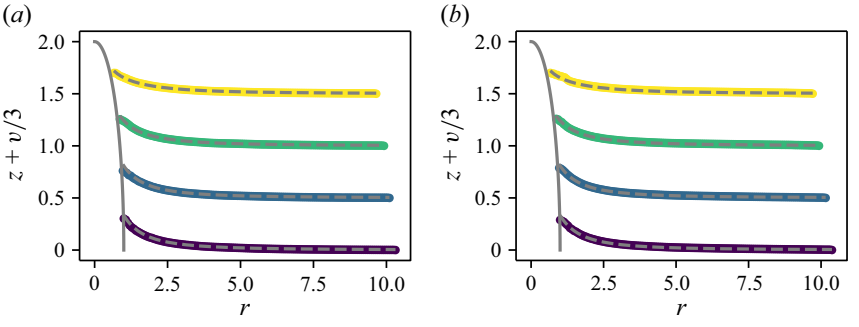

Figure 8. Theoretical and experimental azimuthal velocity radial profiles around a rotating prolate spheroid. Circles are PIV measurements. Each dashed line is the analytical base flow at that height; there is no fitting parameter. The base flow depends only on the aspect ratio. The profiles are shifted by their height and scaled by a factor of 1/3 to distinguish them. From dark to light, the heights are $z = 0$, 0.5, 1 and 1.5 with (*a*) $Ro = \infty$, $Re = 670$, $Fr = 0.320$, $\Lambda = 2$ and (*b*) $Ro = 6$, $Re = 838$, $Fr = 0.288$, $\Lambda = 2$.

Furthermore, the velocity on the ellipsoid, i.e. at $\mu = \sinh^{-1}(1/a)$, is equal to $v = r$ because of the $\sin\theta$ dependence.

Figure 7 shows a colourmap of the velocity field around a spinning spheroid. The top region is an experimental interpolation from profiles at different heights. The bottom region is the theoretical velocity computed from (5.1). There is no global rotation on the left and co-rotation on the right. There is a very good agreement between the experiments and the theory in both cases. Those two experiments illustrate the theoretical result that the azimuthal velocity is independent of the Rossby number.

Similarly to the results for a spinning sphere, experimental validation of the flow up to 8 radii is shown in figure 8. At each height the velocity is plotted and compared with the theoretical velocity. There is an excellent agreement between the experiments and the theory at every height in both cases $Ro = \infty$ and $Ro = 6$.

As for the sphere, the pressure can be obtained by writing $(\partial p/\partial r)_z$ using spheroidal coordinates, as given by (A3). The radial component of the Navier–Stokes equation (3.8)

is thus written

$$\left(\frac{\partial p}{\partial \mu}\right)_z = \frac{v}{\sin\theta}\left(\cosh\mu - \frac{z^2}{a^2\cosh^3\mu}\right)\left(\frac{v}{\sin\theta\sinh\mu} + \frac{2a}{Ro}\right). \tag{5.3}$$

Since the velocity profile (5.1) is proportional to $\sin\theta$, the term $\sin\theta$ disappears from the right-hand side of (5.3), which is a function of μ and z. It can be integrated in μ at constant z to get the pressure:

$$\begin{aligned} p = v_a^2\big[&\tanh^{-1}(1/\cosh\mu)\big(-\cosh\mu + 3z^2/\big(a^2\cosh\mu\big)\big) \\ &+ \big(\tanh^{-1}(1/\cosh\mu)\big)^2/2 \times \big(1 - 3z^2/a^2 + (\cosh\mu)^2 + z^2/\big(a(\cosh\mu)^2\big)\big) \\ &+ 1/2\big(z^2/a^2 - 1 + 8z^2/a^2\ln(\tanh(\mu))(\sinh\mu)^2\big)/(\sinh\mu)^2 + 1/2\big] \\ &+ 2/Ro \times a v_a/4\big[2\cosh\mu + 3\big(1 - 2z^2/a^2\big)\ln(\tanh(\mu/2)) \\ &- 6z^2/\big(a^2\cosh\mu\big) - \tanh^{-1}(1/\cosh\mu)\big(\cosh(2\mu) + 2z^2/(a\cosh\mu)^2\big)\big]. \end{aligned} \tag{5.4}$$

The pressure can then be rewritten as a function of μ and r only by rewriting z^2 as $a^2\cosh^2\mu - r^2\coth^2\mu$. This expression can then be derived with respect to μ at constant r to get the pressure gradient term $(\partial p/\partial z)_r$ in (3.9) using the relation (A7). The density has a simple form:

$$\begin{aligned} \rho = -Fr^2\cos\theta\,\big[&2v_a^2\,\big(\coth\mu/\sinh\mu - 4\ln(\coth\mu)\cosh\mu \\ &+ \tanh^{-1}(1/\cosh\mu)(2 - \tanh^{-1}(1/\cosh\mu)\cosh\mu)\big) \\ &+ \frac{4v_a}{Ro}(\cosh\mu\tanh^{-1}(1/\cosh\mu) - 1)\big], \end{aligned} \tag{5.5}$$

$$\rho = -Fr^2\cos\theta\cosh\mu\left[2v_a^2\left(\frac{1}{\sinh^2\mu} - 4\ln(\coth\mu) + \frac{2T}{\cosh\mu} - T^2\right) + \frac{4v_a}{Ro}\left(T - \frac{1}{\cosh\mu}\right)\right], \tag{5.6}$$

where $T = \tanh^{-1}(1/\cosh\mu)$.

Isopycnals around a spinning prolate spheroid according to (5.6) are shown in figure 9. The influence of Fr and Ro is the same as shown in figure 5. The greater aspect ratio inhibits overall the bending of isopycnals. Let us note that (5.1) and (5.6) recover the flow around a cylinder (Riedinger *et al.* 2011) (a sphere) in the limit $\Lambda \to \infty$ ($\Lambda \to 1^+$).

5.2. *Oblate spheroid*

The same ideas are applied for an oblate spheroid, using the oblate spheroid coordinates (μ, θ, ϕ) with $r = a\cosh\mu\sin\theta$ and $z = a\sinh\mu\sin\theta$, where $a = \sqrt{1 - \Lambda^2}$ is the radius of the spheroid focal ring. The velocity profile is once again given by (Jeffery 1915)

$$v = v_a\left[\arctan\left(\frac{1}{\sinh\mu}\right)\cosh\mu - \tanh\mu\right]\sin\theta \quad \text{with} \quad v_a = \frac{1}{\arctan(a/\Lambda)/a - \Lambda}. \tag{5.7}$$

Figure 10(*a*) shows a colourmap of the velocity field around a spinning spheroid. In this section we only present experimental results for one Ro number as its effect has been discussed in previous sections and is there identical. The top region is an experimental interpolation from profiles at different heights. The bottom region is the theoretical velocity computed from (5.1). There is a good agreement between the experiments and the theory far from the spheroid.

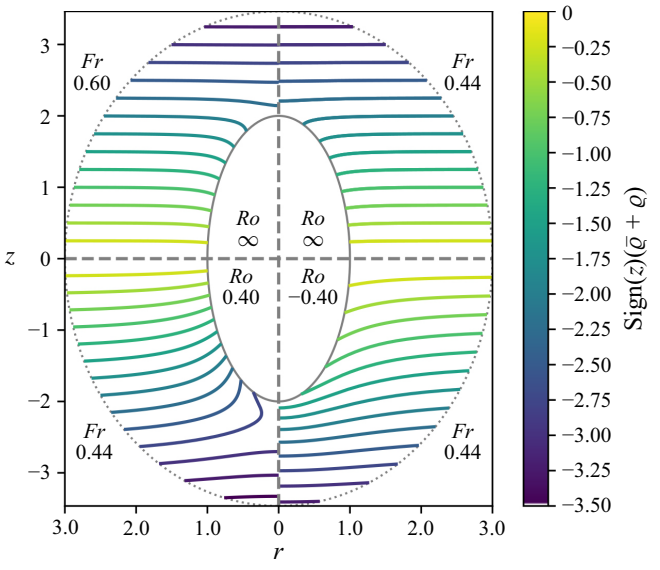

Figure 9. Theoretical isopycnals from (5.6) around a spinning prolate spheroid of aspect ratio $\Lambda = 2$ for four sets of Ro and Fr values. Each quadrant corresponds to a pair of Ro and Fr. In the upper (lower) region the density is increasing (decreasing) from dark to light. The dotted outer ellipse is not a boundary but only the end of the plotting region.

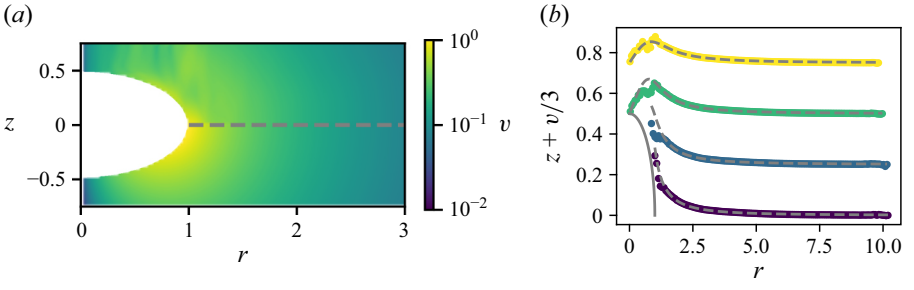

Figure 10. Parameters $Ro = \infty$, $Re = 586$, $Fr = 0.244$, $\Lambda = 0.5$. (*a*) Velocity colourmap around a spinning oblate spheroid. The bottom region is the theoretical base flow computed from (5.7). The top region is an interpolation of experimental velocity profiles at different heights. (*b*) Theoretical and experimental azimuthal velocity radial profiles around a rotating oblate spheroid. Circles are PIV measurements. From dark to light, $z = 0,\ 0.25,\ 0.5$ and 0.75. Each dashed line is the analytical base flow at that height; there is no fitting parameter. The base flow depends only on the aspect ratio. The profiles are shifted by their height and scaled by a factor of 1/3 to distinguish them.

Experimental validation of the flow up to 8 radii is once again shown in figure 10(*b*). At each height the velocity is plotted and compared with the theoretical velocity. There is a good agreement between the experiments and the theory at every height for $r > 1$. The discrepancies between theory and experiments for $r < 1$ can be explained by the perturbation of the PIV signal by the surface of the spheroid illuminated by the laser. The perturbation is greater when the laser illuminates the flatter surface of the oblate spheroid compared with a sphere or a prolate spheroid.

As for the prolate spheroid, the pressure can be obtained by writing $(\partial p/\partial r)_z$ using spheroidal coordinates, as given by (A4). The radial component of the Navier–Stokes equation (3.8) can be integrated in μ at constant z to get the pressure:

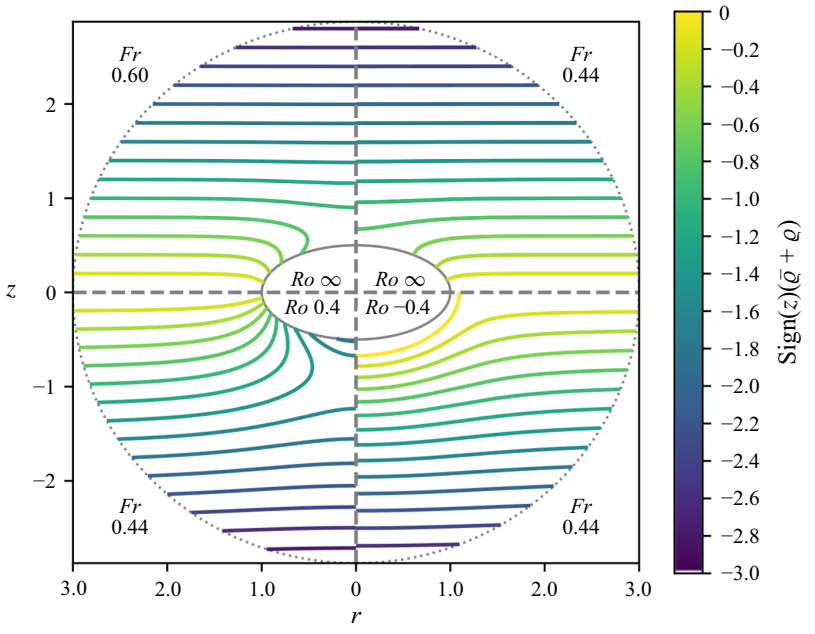

Figure 11. Theoretical isopycnals from (5.10) around a spinning prolate spheroid of aspect ratio $A = 1/2$ for four sets of Ro and Fr values. Each quadrant corresponds to a pair of Ro and Fr. In the upper (lower) region the density is increasing (decreasing) from dark to light. The dotted outer ellipse is not a boundary but only the end of the plotting region.

$$\begin{aligned} p = v_a^2/2\big[&\big(1 - \arctan(1/\sinh\mu)\big(-1 - 6z^2/a^2 + \cosh(2\mu)\big)/\sinh\mu\big) \\ &+ (\arctan(1/\sinh\mu))^2/2\big(-3 - 6z^2/a^2 + \cosh(2\mu) - 2z^2/a^2(\sinh\mu)^{-2}\big) \\ &+ 8z^2/a^2\ln(\tanh(\mu)) + \big(1 + z^2/a^2\big)(\cosh\mu)^{-2}\big] \\ &+ 2/Ro \times a v_a/8\big[\arctan(1/\sinh\mu)\big(2\cosh(2\mu) - 6 - 12z^2/a^2\big) \\ &+ \big(3 + 12z^2/a^2 - 1/\sinh\mu\big(4z^2/a^2\arctan(1/\sinh\mu) + \sinh(3\mu)\big)/\sinh\mu\big)\big]. \end{aligned} \tag{5.8}$$

The pressure can then be rewritten as a function of μ and r only by rewriting z^2 as $a^2\sinh^2\mu - r^2\tanh^2\mu$. This expression can then be derived with respect to μ at constant r to get the pressure gradient term $(\partial p/\partial z)_r$ in (3.9) using the relation (A8). The density has a simple form:

$$\begin{aligned} \rho = -Fr^2\cos\theta\big[&2v_a^2/a(\tanh\mu/\cosh\mu - 4\ln(\coth\mu)\sinh\mu \\ &+ \arctan(1/\sinh\mu)(2 - \arctan(1/\sinh\mu)\sinh\mu)) \\ &+ \frac{4v_a}{Ro}(1 - \sinh\mu\arctan(1/\sinh\mu))\big], \end{aligned} \tag{5.9}$$

$$\begin{aligned} \rho = -Fr^2\cos\theta\sinh\mu\Bigg[&\frac{2v_a^2}{a}\left(\frac{1}{\cosh^2\mu} - 4\ln(\coth\mu) + \frac{2A}{\sinh\mu} - A^2\right) \\ &+ \frac{4v_a}{Ro}\left(\frac{1}{\sinh\mu} - A\right)\Bigg], \end{aligned} \tag{5.10}$$

where $A = \arctan(1/\sinh\mu)$.

Isopycnals around a spinning prolate spheroid according to (5.10) are shown in figure 11. The influence of Fr and Ro is the same as shown in figure 5. The smaller aspect ratio exacerbates overall the bending of isopycnals. Let us note that (5.7) and (5.10) also recover the flow around a disk (a sphere) in the limit $\Lambda \to \infty$ ($\Lambda \to 1^-$).

6. Conclusion

To conclude, we have demonstrated that solids of revolution spinning in a rotating stratified medium can induce an axisymmetric azimuthal time-independent flow around them regardless of the Reynolds number because of the stratification. We have proposed a simple set of equations to solve for any solid of revolution. We analytically solved them in the cases of a rotating spheroid of aspect ratio ranging from $+\infty$ to 0. We have shown that for arbitrary Reynolds numbers this flow is actually equal to the flow computed in the Stokes limit by Jeffery (1915) for a homogeneous fluid. This is made possible by the equilibrium of the pressure gradients induced by the advective and Coriolis terms and the density gradients. This is only possible in stratified fluids. We have experimentally verified these flows for different Λ, Fr and Ro values. We proposed a theoretical model for the spin-up of a rotating sphere and verified it experimentally. In the absence of any destabilisation mechanism, the same diffusive behaviour should hold true with background rotation for different aspect ratios and could be theoretically computed and experimentally checked for prolate and oblate spheroids in further studies. The theoretical profiles enable one to compute local instability criteria to describe when these axisymmetric flows will eventually destabilise. The destabilisation of this flow will be the focus of future studies.

Acknowledgements. The authors thank É. Deléage for his contribution to the analytical computation.

Declaration of interests. The authors report no conflict of interest.

Appendix A.

In order to find the pressure from (3.8), we need to calculate the term $(\partial p/\partial r)_z$ in spherical coordinates and in spheroidal coordinates. The idea is to change from the variables (r, z) to the mixed variables $(\tilde{\mu}, \tilde{z})$ with $\tilde{z} = z$ and $\tilde{\mu} = \mu$. The left-hand side of (3.8) is equal to

$$\left(\frac{\partial p}{\partial r}\right)_z = \left(\frac{\partial p}{\partial \tilde{\mu}}\right)_{\tilde{z}} \left(\frac{\partial \tilde{\mu}}{\partial r}\right)_z + \left(\frac{\partial p}{\partial \tilde{z}}\right)_{\tilde{\mu}} \left(\frac{\partial \tilde{z}}{\partial r}\right)_z . \tag{A1}$$

The second term vanishes because $(\partial \tilde{z}/\partial r)_z = 0$.

In spherical coordinates, the first term can be found by differentiating $\tilde{\mu}^2 = r^2 + z^2$ with respect to r at constant z, to find $(\partial \tilde{\mu}/\partial r)_z = \sqrt{\tilde{\mu}^2 - \tilde{z}^2}/\tilde{\mu}$ such that the pressure term in (3.8) can be written in a simple form:

$$\left(\frac{\partial p}{\partial r}\right)_z = \sin\theta \left(\frac{\partial p}{\partial \tilde{\mu}}\right)_{\tilde{z}} , \tag{A2}$$

where $\sin\theta$ is a simple notation for $\sqrt{\tilde{\mu}^2 - \tilde{z}^2}/\tilde{\mu}$ in these variables $(\tilde{\mu}, \tilde{z})$.

In prolate spheroidal coordinates, the first term can be found by differentiating $r^2/\sinh^2\tilde{\mu} + z^2/\cosh^2\tilde{\mu} = a^2$ with respect to r at constant z, to find $(\partial \tilde{\mu}/\partial r)_z = a \sin\theta/\cosh\mu/(a^2 - z^2/\cosh^4\mu)$ such that the pressure term in (3.8) is equal to

$$\left(\frac{\partial p}{\partial r}\right)_z = \frac{\sin\theta/a}{\cosh\mu - z^2/a^2/\cosh^3\mu} \left(\frac{\partial p}{\partial \tilde{\mu}}\right)_{\tilde{z}} . \tag{A3}$$

In oblate spheroidal coordinates, the first term can be found by differentiating $r^2/\cosh^2\tilde{\mu} + z^2/\sinh^2\tilde{\mu} = a^2$ with respect to r at constant z, to find $(\partial\tilde{\mu}/\partial r)_z = a\sin\theta/\sinh\mu/(a^2 + z^2/\sinh^4\mu)$ such that the pressure term in (3.8) is equal to

$$\left(\frac{\partial p}{\partial r}\right)_z = \frac{\sin\theta/a}{\sinh\mu + z^2/a^2/\sinh^3\mu}\left(\frac{\partial p}{\partial\tilde{\mu}}\right)_{\tilde{z}}. \tag{A4}$$

The same type of calculation must be done to get the density from (3.9). To calculate the term $(\partial p/\partial z)_r$ in spherical coordinates and in spheroidal coordinates, we need to change from the variables (r, z) to the mixed variables $(\hat{\mu}, \hat{r})$ with $\hat{r} = r$ and $\hat{\mu} = \mu$. The left-hand side of (3.9) is equal to

$$\left(\frac{\partial p}{\partial z}\right)_r = \left(\frac{\partial p}{\partial\hat{\mu}}\right)_{\hat{r}}\left(\frac{\partial\hat{\mu}}{\partial z}\right)_r + \left(\frac{\partial p}{\partial\hat{r}}\right)_{\tilde{\mu}}\left(\frac{\partial\hat{r}}{\partial z}\right)_r. \tag{A5}$$

The second term vanishes because $(\partial\hat{r}/\partial z)_r = 0$.

In spherical coordinates, the first term can be found by differentiating $\hat{\mu}^2 = r^2 + z^2$ with respect to z at constant r, to find $(\partial\hat{\mu}/\partial z)_r = \sqrt{\mu^2 - r^2}/\mu = \cos\theta$ such that the pressure term in (3.8) is simply equal to

$$\left(\frac{\partial p}{\partial z}\right)_r = \cos\theta\left(\frac{\partial p}{\partial\hat{\mu}}\right)_{\hat{r}} \tag{A6}$$

in spherical coordinates.

In prolate spheroidal coordinates, the first term can be found by differentiating $r^2/\sinh^2\hat{\mu} + z^2/\cosh^2\hat{\mu} = a^2$ with respect to z at constant r, to find $(\partial\hat{\mu}/\partial z)_r = a\cos\theta/\sinh\mu/(a^2 + r^2/\sinh^4\mu)$ such that the pressure term in (3.8) is simply equal to

$$\left(\frac{\partial p}{\partial z}\right)_r = \frac{\cos\theta/a}{\sinh\mu + r^2/a^2/\sinh^3\mu}\left(\frac{\partial p}{\partial\hat{\mu}}\right)_{\hat{r}}. \tag{A7}$$

In oblate spheroidal coordinates, the first term can be found by differentiating $r^2/\cosh^2\hat{\mu} + z^2/\sinh^2\hat{\mu} = a^2$ with respect to z at constant r, to find $(\partial\hat{\mu}/\partial z)_r = a\cos\theta/\cosh\mu/(a^2 - r^2/\cosh^4\mu)$ such that the pressure term in (3.8) is simply equal to

$$\left(\frac{\partial p}{\partial z}\right)_r = \frac{\cos\theta/a}{\cosh\mu - r^2/a^2/\cosh^3\mu}\left(\frac{\partial p}{\partial\hat{\mu}}\right)_{\hat{r}}. \tag{A8}$$

References

Armi, L., Hebert, D., Oakey, N., Price, J.F., Richardson, P.L., Rossby, H.T. & Ruddick, B. 1989 Two years in the life of a Mediterranean salt lens. *J. Phys. Oceanogr.* **19** (3), 354–370.

Aubert, O., Le Bars, M., Le Gal, P. & Marcus, P.S. 2012 The universal aspect ratio of vortices in rotating stratified flows: experiments and observations. *J. Fluid Mech.* **706**, 34–45.

Bashmachnikov, I., Neves, F., Calheiros, T. & Carton, X. 2015 Properties and pathways of Mediterranean water eddies in the Atlantic. *Prog. Oceanogr.* **137**, 149–172.

Beckers, M., Verzicco, R., Clercx, H.J.H. & Van Heijst, G.J.F. 2001 Dynamics of pancake-like vortices in a stratified fluid: experiments, model and numerical simulations. *J. Fluid Mech.* **433**, 1–27.

Burin, M.J., Sommeria, J. & Viboud, S. 2020 Instabilities and layering of a heated laboratory anticyclone. *Phys. Rev. Fluids* **5** (6), 063801.

Carton, X., Le Cann, B., Serpette, A. & Dubert, J. 2013 Interactions of surface and deep anticyclonic eddies in the Bay of Biscay. *J. Mar. Syst.* **109–110**, S45–S59.

Chang, K.I., Teague, W.J., Lyu, S.J., Perkins, H.T., Lee, D.K., Watts, D.R., Kim, Y.B., Mitchell, D.A., Lee, C.M. & Kim, K. 2004 Circulation and currents in the southwestern East/Japan Sea: overview and review. *Prog. Oceanogr.* **61** (2), 105–156.

FLÓR, J.B., HIRSCHBERG, L., OOSTENRIJK, B.H. & VAN HEIJST, G.J.F. 2018 Onset of centrifugal instability at a rotating cylinder in a stratified fluid. *Phys. Fluids* **30** (8), 084103.

GRIFFITHS, R.W. & LINDEN, P.F. 1981 The stability of vortices in a rotating, stratified fluid. *J. Fluid Mech.* **105**, 283–316.

HUA, B.L., MÉNESGUEN, C., LE GENTIL, S., SCHOPP, R., MARSSET, B. & AIKI, H. 2013 Layering and turbulence surrounding an anticyclonic oceanic vortex: *in situ* observations and quasi-geostrophic numerical simulations. *J. Fluid Mech.* **731**, 418–442.

PAILLET, J., LE CANN, B., CARTON, X., MOREL, Y. & SERPETTE, A. 2002 Dynamics and evolution of a Northern Meddy. *J. Phys. Oceanogr.* **32** (1), 55–79.

JEFFERY, G.B. 1915 On the steady rotation of a solid of revolution in a viscous fluid. *Proc. Lond. Math. Soc.* **2** (1), 327–338.

KLOOSTERZIEL, R.C., CARNEVALE, G.F. & ORLANDI, P. 2007 Inertial instability in rotating and stratified fluids: barotropic vortices. *J. Fluid Mech.* **583**, 379–412.

LE BARS, M. 2021 Numerical study of the McIntyre instability around Gaussian floating vortices in thermal wind balance. *Phys. Rev. Fluids* **6** (9), 093801.

LE BARS, M. & LE GAL, P. 2007 Experimental analysis of the stratorotational instability in a cylindrical Couette flow. *Phys. Rev. Lett.* **99** (6), 064502.

MARCUS, P.S. & TUCKERMAN, L.S. 1987 Simulation of flow between concentric rotating spheres. Part 1. Steady states. *J. Fluid Mech.* **185**, 1–30.

MESCHANOV, S.L. & SHAPIRO, G.I. 1998 A young lens of Red Sea Water in the Arabian Sea. *Deep Sea Res. I: Oceanogr. Res. Papers* **45** (1), 1–13.

MOLEMAKER, M.J., MCWILLIAMS, J.C. & CAPET, X. 2010 Balanced and unbalanced routes to dissipation in an equilibrated Eady flow. *J. Fluid Mech.* **654**, 35–63.

NAYAR, K.G., SHARQAWY, M.H., BANCHIK, L.D. & LIENHARD V, J.H. 2016 Thermophysical properties of seawater: a review and new correlations that include pressure dependence. *Desalination* **390**, 1–24.

RICHARDSON, P.L., BOWER, A.S. & ZENK, W. 2000 A census of Meddies tracked by floats. *Prog. Oceanogr.* **45** (2), 209–250.

RIEDINGER, X., LE DIZÈS, S. & MEUNIER, P. 2011 Radiative instability of the flow around a rotating cylinder in a stratified fluid. *J. Fluid Mech.* **672**, 130–146.

RUDDICK, B. & HEBERT, D. 1988 The mixing of Meddy 'Sharon'. In *Elsevier Oceanography Series*, (ed. Nihoul, J.C.J. & Jamart, B.M.), Small-Scale Turbulence and Mixing in the Ocean, vol. 46, pp. 249–261. Elsevier.

SAUNDERS, P.M. 1973 The instability of a baroclinic vortex. *J. Phys. Oceanogr.* **3** (1), 61–65.

SMYTH, W.D. & MCWILLIAMS, J.C. 1998 Instability of an axisymmetric vortex in a stably stratified, rotating environment. *Theor. Comput. Fluid Dyn.* **11** (3), 305–322.

SUTYRIN, G.G. & RADKO, T. 2017 The fate of pancake vortices. *Phys. Fluids* **29** (3), 031701.

TOKOS, K.S. & ROSSBY, T. 1991 Kinematics and dynamics of a Mediterranean salt lens. *J. Phys. Oceanogr.* **21** (6), 879–892.

YIM, E. & BILLANT, P. 2015 On the mechanism of the Gent–McWilliams instability of a columnar vortex in stratified rotating fluids. *J. Fluid Mech.* **780**, 5–44.

YIM, E., BILLANT, P. & MÉNESGUEN, C. 2016 Stability of an isolated pancake vortex in continuously stratified-rotating fluids. *J. Fluid Mech.* **801**, 508–553.